Zi-ru Li
Wuhan University of Technology,
Hubei 430063 China;
Delft University of Technology,
Delft 6700 AA, The Netherlands
e-mail: lisayhw333@hotmail.com

Mathieu Pourquie
Delft University of Technology,
Delft 6700 AA, The Netherlands
e-mail: M.J.B.M.Pourquie@tudelft.nl

Tom van Terwisga[1]
Delft University of Technology
Delft 6700 AA, The Netherlands;
Maritime Research Institute Netherlands (MARIN),
Wageningen 6700 AA, The Netherlands
e-mail: t.v.terwisga@marin.nl

Assessment of Cavitation Erosion With a URANS Method

An assessment of the cavitation erosion risk by using a contemporary unsteady Reynolds-averaged Navier–Stokes (URANS) method in conjunction with a newly developed postprocessing procedure is made for an NACA0015 hydrofoil and an NACA0018-45 hydrofoil, without the necessity to compute the details of the actual collapses. This procedure is developed from detailed investigations on the flow over a hydrofoil. It is observed that the large-scale structures and typical unsteady dynamics predicted by the URANS method with the modified shear stress transport (SST) k-ω turbulence model are in fair agreement with the experimental observations. An erosion intensity function for the assessment of the risk of cavitation erosion on the surface of hydrofoils by using unsteady RANS simulations as input is proposed, based on the mean value of the time derivative of the local pressure that exceeds a certain threshold. A good correlation is found between the locations with a computed high erosion risk and the damage area observed from paint tests. [DOI: 10.1115/1.4026195]

Keywords: multiphase URANS method, unsteady cavitation, Reboud's correction, cavitation erosion, erosion intensity function

1 Introduction

A cavitating flow is a complicated multiphase flow involving phase change, compressibility, viscous effects, and turbulent fluctuations. It is a common phenomenon that often occurs in the flow over propulsion systems, rudders, and other hydraulic machinery. Due to the limitations imposed on the attainable propulsor thrust and efficiency by cavitation-induced vibrations and cavitation erosion risk, it becomes essential to predict cavitation and assess cavitation hindrance in an early design stage.

Among all adverse effects of cavitation, cavitation erosion is the most complex since it involves multiscale hydrodynamic processes combined with the response of solid material that is exposed to the cavitating flow. Predicting the quantitative cavitation aggressiveness and the most likely location of cavitation erosion are complex problems that have motivated an important amount of basic and applied research in the fields of hydrodynamics, mechanical engineering, and metallurgy. From an industrial point of view, the evaluation of the erosive power of cavitating flows and prediction of the material damage remains a major concern for both the design and maintenance stage.

A wide range of studies that deal with problems from bubble dynamics to material testing have been made (e.g., Refs. [1–5]), all aiming toward a deeper understanding of these phenomena. Recently, a number of attempts to predict the cavitation erosion risk were published [6–9] where the predictions were based on visual observations and computational fluid dynamics (CFD) tools. Although much is known about the individual bubble dynamics and the material reaction, no reliable successful numerical prediction method for cavitation erosion has thus far been developed, which involves all elements of cavitation erosion. It is still a big challenge to numerically predict the risk of cavitation erosion without the support of model tests.

Van Terwisga et al. [10] hypothesized that the erosive action by cavitation is largely caused by the acoustic shock waves that are released upon collapse of a focused cavity. This hypothesis builds further on the fundamental work done on cavitation erosion by Bark et al. [11]. It is suggested here that the focusing of potential energy in the cavity is occurring through large-scale vortices occurring in the breakup region of sheet cavitation. This paper focuses on the question whether the conditions for erosive cavitation can be predicted from an unsteady RANS method, without the necessity to compute the details of the actual collapse. This would then justify a focus on modeling efforts of essentially the large-scale cavity dynamics only.

At first, a frequently used NACA0015 hydrofoil at 6 deg angle of attack, which is often used as a standard test case [12–15], is adopted to investigate the adequacy of the URANS method implemented in FLUENT applying the SST k-ω turbulence model for cavitating flows in a 2D computational domain. Calculations are performed for two cavitating conditions with specific cavitation regimes characterized by $\sigma = 1.6$, showing a steady cavitating flow, and $\sigma = 1.0$, showing relatively strong dynamic shedding. These cases are primarily used for testing of input and control parameters, such as the influence of grid density and the numerical interpolation schemes.

The results indicate that the breakup of the sheet cavity and also the periodic shedding of the cloud cavity at the trailing edge of the sheet can only be predicted by an artificial reduction of the turbulent viscosity in the regions of higher vapor volume fraction as suggested by Reboud et al. [16]. Coutier-Delgosha et al. [17] suggested that Reboud's correction accounts for the compressibility effects on the turbulence model. However, it is noted that other RANS codes such as Star-CD [12] and FreSCo [13] do not need this viscous correction for the NACA0015 hydrofoil. For the Delft Twist-11 hydrofoil used as a common test case in the SMP2011workshop [18], only steady or at most a "breathing" behavior was observed by all the participants applying a URANS method unless Reboud's correction is applied, where unsteady dynamics was actually observed in the experiments. It is also noted that for the unsteady simulation, the number of iterations per time step should be carefully selected to avoid a lack of numerical convergence.

Subsequently, calculations are performed for unsteady cavitating flow over an NACA0015 hydrofoil at 8 deg angle of attack in a 3D computational domain by using the numerical approach following the guidelines obtained from the 2D simulations. The simulation results are then compared with experimental results from a high speed cavitation tunnel [19]. The large-scale structures and typical unsteady cavity dynamics are qualitatively well captured by the URANS method compared with the experimental

[1]Corresponding author.

Contributed by the Fluids Engineering Division of ASME for publication in the JOURNAL OF FLUIDS ENGINEERING. Manuscript received December 20, 2012; final manuscript received December 3, 2013; published online February 28, 2014. Assoc. Editor: Olivier Coutier-Delgosha.

observations, such as the breakup of the sheet cavity, the formation of the re-entrant jet, and the formation of the horseshoe-shaped cloudy cavity due to side-entrant flow and its collapse.

Finally, the qualitative correlation between the risk of cavitation erosion and unsteady cavitation phenomena has been investigated by postprocessing the unsteady RANS results for the test case of an NACA0015 hydrofoil and an NACA0018-45 hydrofoil. Among several criteria suggested by an analysis of the potential power that is stored in the vapor structure, the time derivative of the local pressure $\partial p/\partial t$ shows the best correlation with the observed damaged areas [20]. A new erosion intensity function is then presented based on the mean of $\partial p/\partial t$ values that exceed a certain threshold. A good correlation has been found between the predicted locations with high erosion risk and the damaged area observed from paint tests for the two different foils.

2 Numerical Models

2.1 Governing Equations. The governing equations for a two-phase flow are based on a single-fluid approach, regarding the mixture as one liquid. The flow field is solved for the mixture continuity and momentum equations:

$$\frac{\partial}{\partial t}(\rho_m) + \frac{\partial}{\partial x_i}(\rho_m u_i) = 0 \tag{1}$$

$$\frac{\partial}{\partial t}(\rho_m u_i) + \frac{\partial}{\partial x_j}(\rho_m u_i u_j) = -\frac{\partial p}{\partial x_i} + \frac{\partial \tau_{ij}}{\partial x_j} + f_i \tag{2}$$

where p is the pressure, f_i and u_i are the body force and velocity in the i direction, and τ_{ij} denotes the viscous tensor, which can be expressed as

$$\tau_{ij} = \mu_m \left[\left(\frac{\partial u_i}{\partial x_j} + \frac{\partial u_j}{\partial x_i} \right) - \frac{2}{3}\delta_{ij}\frac{\partial u_k}{\partial x_k} \right] \tag{3}$$

Here the relationship between the mixture density ρ_m, mixture viscosity μ_m, and the vapor volume fraction α is defined as

$$\rho_m = \alpha\rho_v + (1-\alpha)\rho_l \tag{4}$$

$$\mu_m = \alpha\mu_v + (1-\alpha)\mu_l \tag{5}$$

where the subscripts m, v and l represent mixture, vapor, and liquid phase, respectively.

2.2 Turbulence Modeling. Experience has taught us that turbulence models play a key role in the numerical simulation of cavitating flows, especially for the unsteady dynamics. The SST k-ω turbulence model developed by Menter [21] is adopted in this study, which is a blending between the k-ω model in the near-wall region and the k-ε model in the far field. The refinements can make this model behave properly in both the near-wall and the far-field zones.

To improve the cavity dynamics in the simulation, a modification of the turbulent viscosity μ_t is applied following the idea of Reboud et al. [16]:

$$\mu_t = f(\rho) C_\omega \frac{k}{\omega} \tag{6}$$

$$f(\rho) = \rho_v + \frac{(\rho_m - \rho_v)^n}{(\rho_l - \rho_v)^{n-1}}; \quad n \gg 1 \tag{7}$$

With a recommended exponent value $n = 10$, the turbulent viscosity in the region with higher vapor volume fraction is reduced so as to better simulate the re-entrant jet and shedding behavior.

2.3 Cavitation Modeling. The cavitation model adopted here was developed by Schnerr and Sauer [22]. The conservation equation for the vapor volume fraction has the general form

$$\frac{\partial}{\partial t}(\alpha\rho_v) + \nabla \cdot (\alpha\rho_v \vec{u}) = S_e - S_c \tag{8}$$

where the source terms S_e and S_c refer to the evaporation and condensation of the vapor bubbles, respectively, accounting for the mass transfer between the vapor and liquid phases in cavitation.

The source terms are derived from the Rayleigh–Plesset equation and are defined as

$$S_e = \frac{\rho_v \rho_l}{\rho_m}\alpha(1-\alpha)\frac{3}{R}\sqrt{\frac{2}{3}\frac{(p_v - p)}{\rho_l}}, \text{when} \quad p_v \geq p \tag{9}$$

$$S_c = \frac{\rho_v \rho_l}{\rho_m}\alpha(1-\alpha)\frac{3}{R}\sqrt{\frac{2}{3}\frac{(p - p_v)}{\rho_l}}, \quad \text{when} \quad p_v \leq p \tag{10}$$

The bubble radius can be related to the vapor volume fraction α and the bubble number density n_b as follows:

$$R = \left(\frac{\alpha}{1-\alpha}\frac{3}{4\pi n_b} \right)^{\frac{1}{3}} \tag{11}$$

where n_b is the only parameter to be provided as input for FLUENT with a default value of 1e + 13 [23]. The bubble number density is related to the bubble nuclei distribution in the fluid and is an important parameter for the description of phase transition and mass transfer between two phases. However, it is difficult to acquire such information in advance because complex experiments and sophisticated test facilities are demanded. For the default value of bubble number density, it can be observed that bubbles have a radius within a bandwidth of [0 μm $\sim$10 μm] when the vapor volume fraction is lower than 0.01. We use the default value for all simulations at first due to the unknown spectrum for current test facility in MARIN's high speed tunnel. The influence of this value on the simulation results will be discussed in Sec. 5.3.

2.4 Numerical Solution. For all simulations, a fully coupled solver is used to solve the pressure and momentum equations, which can lead to a more robust calculation and faster convergence than for the segregated solver [23]. The pressure is discretized using the PRESTO! scheme, and the convection term of the momentum equations is discretized by the QUICK scheme with a limiter. The same is done for the convection terms in the turbulence equations and vapor volume fraction equation.

3 Case Description

3.1 2D Computational Domain. For the investigations in the 2D computational domain, the test geometry is an NACA0015 hydrofoil at 6 deg angle of attack with a chord length $C = 200$ mm, which has been taken as the general test subject in the VIRTUE WP4 Workshop. The size of the domain is 1400×570 mm, extending two chord lengths ahead of the leading edge and four chord lengths behind the trailing edge. The grid sensitivity and convergence are investigated on three grids with different densities but with similar multiblock topology: an O-grid around the foil embedded in an H-grid, resulting in a total of 12 blocks. The features of the three grids are listed in Table 1.

Based on previous sensitivity studies [20] on the transient parameters, such as time step size, iteration number per time step, and temporal discretization scheme, the first-order implicit scheme is adopted here and the time step size is estimated by $\Delta t = \Delta x \cdot \text{Courant}/U_{\text{ref}}$ with a characteristic Courant number of 0.50 for coarse grid G3 and 1.0 for fine grid G1. A velocity inlet condition is applied at the upstream inlet. A pressure outlet condition is used at the outlet boundary, where the specified pressure at the outlet can be derived from the cavitation number

Table 1 Grid features of an NACA0015 hydrofoil (*AoA* = 6 deg)

Grid	#Cells	#Edges	Level	y^+
G1	111,232	468	Fine	0.1797
G2	62,568	351	Medium	0.2432
G3	27,808	234	Coarse	0.3747

Table 2 Boundary conditions and fluid properties for an NACA0015 hydrofoil (*AoA* = 6 deg)

Boundary conditions	NACA0015 ($AoA = 6$ deg)	
Mean velocity inlet (m/s)	$V = 6$	
Pressure outlet (kPa)	31.7 ($\sigma = 1.6$)	20.9 ($\sigma = 1.0$)
Turbulence intensity (%)	1	
Turbulent viscosity ratio	10	
Foil	No-slip wall	
Tunnel walls (top and bottom)	Slip wall	
Fluid properties ($T = 24$ °C)	Vapor	Liquid
Density (kg/m^3)	0.023	998
Dynamic viscosity (kg/ms)	9.95×10^{-6}	0.0011
Vapor pressure (kPa)	2.97	

Table 3 Boundary conditions and flow properties for an NACA0015 hydrofoil (*AoA* = 8 deg)

Boundary conditions	NACA0015 ($AoA = 8$ deg)	
Mean velocity inlet (m/s)	$V = 17.3$	
Pressure outlet (kPa)	302.295 ($\sigma = 2.01$)	
Turbulence intensity (%)	1	
Turbulent viscosity ratio	10	
Foil	No-slip wall	
Midspan	Symmetry	
Tunnel walls	No-slip wall	
Fluid properties ($T = 16.3$ °C)	Vapor	Liquid
Density (kg/m^3)	0.01389	998.85
Dynamic viscosity (kg/ms)	9.63×10^{-6}	0.0011
Vapor pressure (kPa)	1.854	

under consideration. The cavitation number is determined here with the outlet pressure as the reference pressure, $\sigma = (p_{\text{out}} - p_v)/(1/2)\rho_l u^2$. The cavitation regimes to be examined correspond to a cavitation number of $\sigma = 1.6$, showing a steady cavitating flow, and $\sigma = 1.0$, showing unsteady shedding. The top and bottom walls are taken as free slip walls. The physical properties of the two phases, liquid and vapor, are taken at a temperature of 24 °C. Detailed initial and boundary conditions as well as the fluid properties are listed in Table 2.

3.2 3D Computational Domain. For the investigations in the 3D computational domain, the test geometry is an NACA0015 hydrofoil at 8 deg angle of attack with a chord length $C = 60$ mm. The domain for the three-dimensional flow is obtained by extruding the 2D geometry in the spanwise direction by half of the width of the hydrofoil, i.e., 20 mm. The grid topology in the chordwise direction is similar as that adopted for the NACA0015 hydrofoil at 6 deg angle of attack but with 3.0 chord-lengths ahead of the leading edge and 5.5 chord-lengths behind the trailing edge of the hydrofoil. Two hundred sixty-four edges are set on the hydrofoil, and the cell size in the wall normal direction is such that $y^+ < 1$.

Similar boundary conditions are applied at the boundaries as for the 2D case. Additionally, on the tunnel walls, a no-slip wall condition is applied, whereas a symmetry condition is applied on the midspan. The unsteady dynamics are investigated for one specific cavitation regime for a cavitation number of $\sigma = 2.01$. A time step size of $\Delta t = 2e - 05s$ is used based on the equation $\Delta t = \Delta x \cdot \text{Courant}/U_{\text{ref}}$ with a courant number around 0.75. The physical properties of the two phases are taken at a temperature of 16.3 °C. The detailed initial and boundary conditions and the fluid properties are listed in Table 3.

Table 4 Test conditions for run no. 26

	Run No. 26
AoA (deg)	8
V (m/s)	17.3
σ	2.01
Re	9.50×10^5

Table 5 Test conditions for NACA0018-45 hydrofoil (*AoA* = 6.5 deg)

	003-04
AoA (deg)	6.5
V (m/s)	24.2
σ	0.72
Re	1.50×10^6

Table 6 Boundary conditions and flow properties for an NACA0018-45 hydrofoil (*AoA* = 6.5 deg)

Boundary conditions	NACA0018-45 ($AoA = 6.5$ deg)	
Mean velocity inlet (m/s)	$V = 24.2$	
Pressure outlet (kPa)	213.115 ($\sigma = 0.72$)	
Turbulence intensity (%)	1	
Turbulent viscosity ratio	10	
Foil	No-slip wall	
Midspan	Symmetry	
Tunnel walls	No-slip wall	
Fluid properties ($T = 23$ °C)	Vapor	Liquid
Density (kg/m^3)	0.021	997.5
Dynamic viscosity (kg/ms)	9.81×10^{-6}	0.00093
Vapor pressure (kPa)	2.811	

The experiments to be compared with the numerical simulations have been performed by MARIN in cooperation with Lloyd's Register [19]. The test conditions for the selected case (run no. 26) resemble the conditions in the numerical simulation, as listed in Table 4.

3.3 Erosion Risk Assessment. An erosion intensity function for the assessment of the cavitation erosion risk on the surface of the hydrofoils, using unsteady RANS simulations as input, is evaluated for the previous test case of an NACA0015 hydrofoil at 8 deg angle of attack in 3D computational domain, as well as for another hydrofoil, namely a nNACA0018-45 hydrofoil at 6.5 deg angle of attack.

An O-H multiblock mesh with 309 edges on the foil has been adopted for the NACA0018-45 hydrofoil. Similar boundary conditions are applied at the boundaries as for the NACA0015 hydrofoil. The unsteady dynamics are investigated for one specific cavitation regime with a cavitation number of $\sigma = 0.72$. The physical properties of the two phases are taken at a temperature of 23 °C, resembling the test conditions for the experiments performed by Van Terwisga [24], as listed in Table 5. The detailed initial and boundary conditions and the flow properties are listed in Table 6.

4 2D Numerical Results

The flow characteristics under steady and unsteady cavitating condition are investigated for the frequently used NACA0015

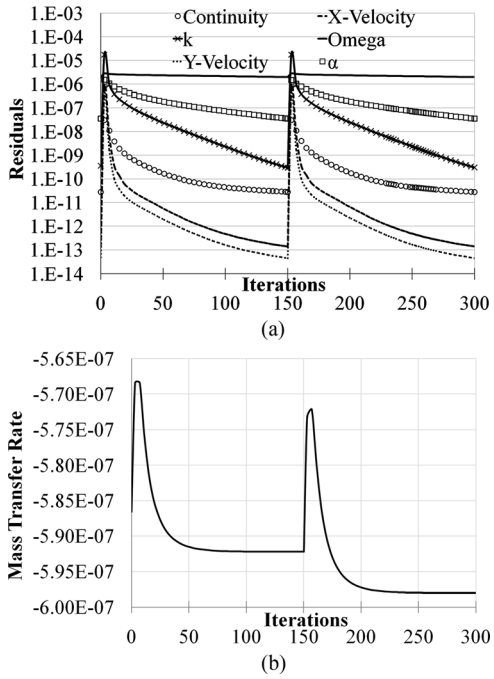

Fig. 1 Time histories of the (*a*) residuals and (*b*) mass transfer rate during two successive time steps for the NACA0015 hydrofoil at 6 deg angle of attack at $\sigma = 1.0$ for the fine grid G1

hydrofoil at 6 deg angle of attack by the URANS code implemented in FLUENT. These results are compared with the results presented at the VIRTUE WP4 Workshop [12–14] to analyze the numerical uncertainty.

4.1 Steady Cavitating Condition. The simulations for steady cavitating condition are conducted with a transient solver. The appropriate iteration number per time step is investigated by checking both the time histories of the residual for each equation and the volume integral of the mass transfer rate through the phase interface, as shown in Fig. 1. It was observed that 100 iterations per time step are demanded for the fine grid G1 to achieve constant mass transfer during each time step, and 60 iterations are needed for the medium grid G2 and the coarse grid G3.

The grid convergence studies are then conducted on three systematically and substantially refined grids (see Table 1). With the recommended Grid Convergence Index (GCI) method proposed by Celik [25] and Celik et al. [26], the lift and drag coefficients and total vapor volume are evaluated over the NACA0015 hydrofoil for a cavitation number of $\sigma = 1.6$. As shown in Table 7, the convergence for the three grids is monotone for the lift and drag coefficients but oscillatory for the total vapor volume. It can be seen that the approximate relative error E_a^{21} and extrapolated relative error E_{ext}^{21} for these quantities between the medium grid G2 and fine grid G1 are very small, and the numerical uncertainty in the fine grid solution GCI_{fine}^{21} is about 0.17% for the drag coefficient, 0.16% for the lift coefficient, and 0.74% for the total vapor volume.

It is concluded that the solutions can be considered to be grid independent under the current resolution, where the maximum y^+ value on the hydrofoil surface is smaller than 1.0. However, from the contours of the instantaneous vapor volume fraction, it is indicated that more details in the cavity structures at the closure of the main cavity can be obtained with the finer grid. It then becomes interesting to see if this is also the case (or even more so) for the unsteady cavitation calculations since then it might have a significant influence on the behavior of the large-scale unsteady dynamics.

Table 7 Numerical uncertainty study for some flow characteristics with different grid densities

	C_d	C_l	V_{cav}	Level
G1	0.01809	0.61166	3.0082×10^{-5}	Fine
G2	0.01807	0.61041	3.0411×10^{-5}	Medium
G3	0.01805	0.60474	2.9104×10^{-5}	Coarse
$E_a(21)$	0.13%	0.20%	1.09%	–
$E_{\text{ext}}(21)$	0.13%	0.13%	0.60%	–
GCI (fine)	0.17%	0.16%	0.74%	–

Table 8 Summary of the numerically obtained frequencies from various sources ($AoA = 6$ deg, $\sigma = 1.0$)

Author	Flow velocity (m/s)	Frequency (Hz)
Sauer [27]	12	≈11
Schnerr et al. [28]	12	≈11.18 (incompressible)
	12	≈9 (compressible)
Koop [29]	12	≈24
Oprea [30]	6	≈14
Hoekstra and Vaz [31]	6	≈15.4

4.2 Unsteady Cavitating Condition. A study of the effect of the modification of the turbulence model on the unsteady dynamics is conducted on the coarse grid G3 at first. It was found that the expected unsteady dynamic shedding would not be triggered unless one applies Reboud's modification for the eddy viscosity in the region of the vapor-liquid interface [14,20,32].

It should be noted that the selection of a proper iteration number per time step was found to be of prime importance when unsteady cavitation phenomena are present because an incomplete calculation for each time step would predict too low a shedding frequency. The default 20 iterations per time step in FLUENT predicts a main natural frequency of 5.4 Hz. This is in disagreement with some published numerically obtained frequencies for the same condition. It is observed that 50 iterations are demanded for the coarse grid. This was checked by monitoring the time histories of the residual for each equation and the volume integral of the mass transfer rate. When the iteration number is increased to 50 iterations per time step, a higher main shedding frequency of 11 Hz is obtained, which is much closer to those published results, as shown in Table 8.

Simulations are then conducted on the fine grid G1 to investigate the influence of the grid density on the capture of the main characteristics of the unsteady dynamics. At least 100 iterations per time step are demanded to obtain a converged mass transfer rate. It is observed that the mean magnitude of the total vapor volume is approximately of the same order for both grids, but there is a small discrepancy in the predicted shedding frequency. For the fine grid, a bit higher value of 11.4 Hz is obtained from the FFT analysis of the time history of the total vapor volume. It is also observed that similar basic unsteady dynamics are captured on both grids, as shown in Fig. 2. The typical cycle can be characterized by the development of the main sheet cavity from the leading edge together with the collapse of large-scale structures near the trailing edge (Fig. 2 ①–③), the rolling-up of vapor structures shed from the breakup sheet cavity (Fig. 2 ④–⑧), and the transformation into large-scale structures that travel further downstream towards the trailing edge (Fig. 2 ⑨–⑫).

Though the refinement in grid density appears to simulate more details, the essential unsteady dynamics can already be captured by adopting the coarse grid G3 in the current topology and resolution. As we mainly focus on the characteristics of the large-scale structures, such as their volume, location, and collapse period, the results predicted by both grids are comparable with each other. It can be concluded that the current approach with a URANS method is capable of predicting the large-scale unsteady dynamics

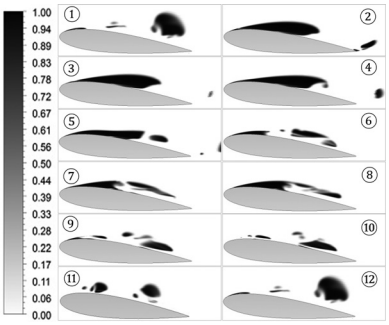

Fig. 2 Contours of the vapor volume fraction during one cycle for a NACA0015 hydrofoil (*AoA* = 6 deg) at $\sigma = 1.0$ with the modified SST *k*-ω turbulence model on fine grid G1

even with the coarse grid, where the maximum y^+ value on the hydrofoil surface is already smaller than 1.0.

5 3D Numerical Results

Experience obtained from the previous analyses for a 2D computational domain will be applied to the simulation of an unsteady cavitating flow over an NACA0015 hydrofoil at 8 deg angle of attack in a 3D domain in this section.

5.1 Typical Unsteady Phenomena. The URANS results with the modified SST *k*-ω turbulence model basically reproduce the features of the shedding process observed in the cavitation tunnel at the selected test condition, such as the detachment of the cloudy cavities from the main sheet cavity and the collapse of the cloudy cavities. The time history of the total vapor volume shows a high-frequency fluctuation ($f \approx 216$ Hz) modulated by an unsteady amplitude characterized by a very low frequency ($f \approx 36$ Hz). It is qualitatively similar as to what has been observed in the 2D computation domain [33].

Typical images obtained by visualizing the isosurface of the instantaneous vapor fraction with a contour value of $\alpha = 0.1$ in top view and downstream view are separately shown in Fig. 3, representing a typical shedding cycle at the high frequency. The observed unsteady phenomena can be characterized as follows:

- The leading edge sheet cavity is growing together with the collapse of the cloudy cavity formed from the last pinch-off (see Fig. 3 ①).
- Re-entrant flow moves upstream towards the leading edge until it breaks the main sheet cavity. The upstream part of the sheet cavity partially disappears from the midspan (see Fig. 3 ②).
- The downstream part of the sheet cavity starts to roll up from the foil surface and forms a cloudy cavity in a cylindrical shape, slightly thicker at the midspan and thinner at the sides of the hydrofoil (see Fig. 3 ③).
- The remaining upstream part of the main sheet cavity prolongs in spanwise location and is subsequently merged into the new sheet cavity that develops from the leading edge again. The cloudy cavity downstream gradually transforms into a horseshoe shape (see Fig. 3 ④,⑤).
- Finally, the cloud cavity collapses downstream and the leading edge sheet cavity extends along the chord length, initiating a new cycle (see Fig. 3 ⑥).

5.2 Breakup of the Sheet Cavity. When comparing the numerical simulation results with the experimental observations, it is found that the synchronization of the collapse of the cloudy cavities and the development and breakup of the leading edge sheet cavity shows a good qualitative match, as shown in Fig. 4.

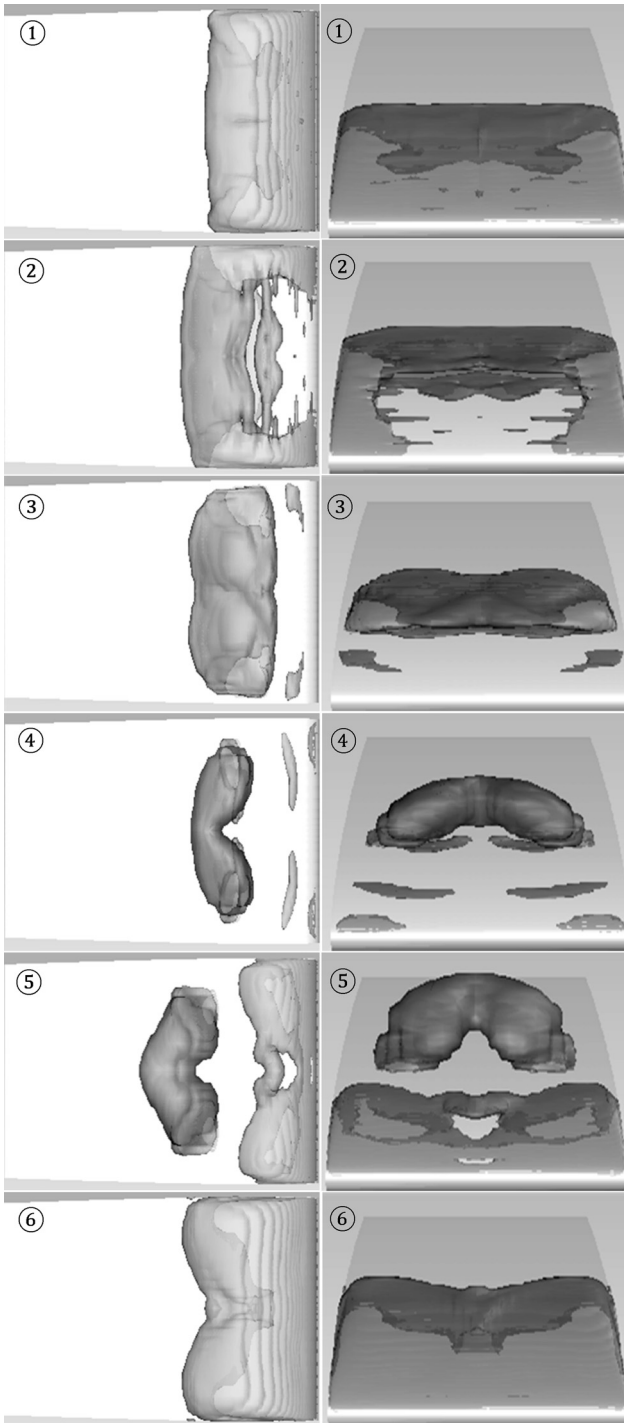

Fig. 3 Sequences of isosurface plots of the instantaneous vapor volume fraction with a contour value of $\alpha = 0.1$ during one typical shedding cycle in (*a*) top view (flow from right to left) and (*b*) downstream view on the NACA0015 hydrofoil (3D representation) with the modified SST *k*-ω turbulence model ($C = 60$ mm, *AoA* = 8 deg, $\sigma = 2.01$, $U = 17.3$ m/s, $P_{out} = 302.295$ kPa, $T = 16.3\,^{\circ}$C)

A typical horseshoe vapor structure has been observed during the experiments as well as in the numerical simulations. It is considered to be at least one of the driving mechanisms for cavitation erosion [34].

Saito et al. [35] simulated a three-dimensional unsteady cavitating flow around an NACA0015 hydrofoil at 8 deg angle of attack

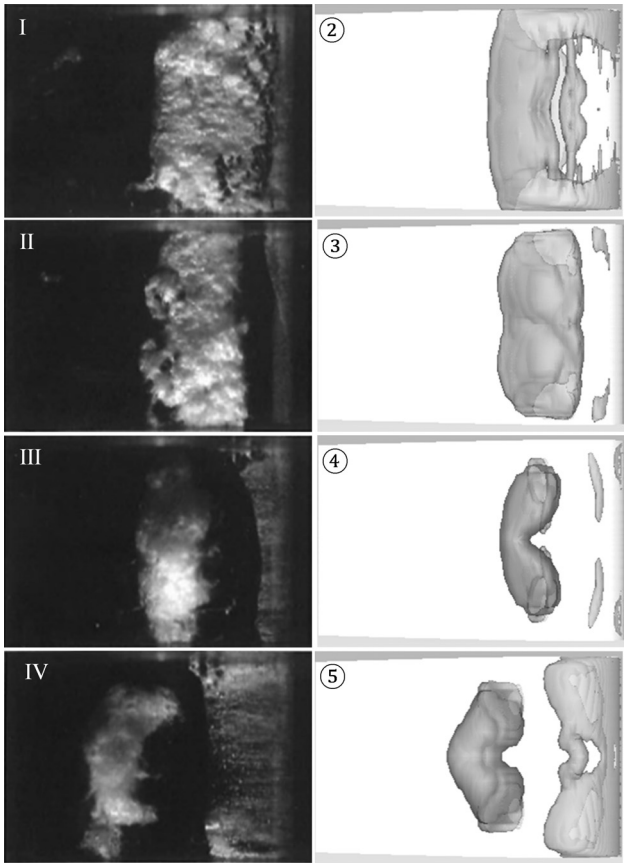

Fig. 4 Comparison between several typical instants obtained by (*a*) experimental observations and (*b*) numerical simulations (isosurface plots of the instantaneous vapor volume fraction with a contour value of $\alpha = 0.1$) for the flow over an NACA0015 hydrofoil (3D representation) with the modified SST k-ω turbulence model (flow from right to left, $C = 60$ mm, $AoA = 8$ deg, $\sigma = 2.01$, $U = 17.3$ m/s, $P_{out} = 302.295$ kPa, $T = 16.3\,^{\circ}$C)

that was fixed between sidewalls and explained that the sidewall effect is an important factor in causing the generation of the horseshoe-shaped cloudy cavity, which is also noted by Van Rijsbergen et al. [19].

The transformation process from a cylindrical shape into a horseshoe shape can be clearly observed during a typical shedding cycle (also see Fig. 3). It can be described as follows:

- The shed cavity at first rolls up in a cylindrical shape that is thicker in the middle and thinner at the sides (see Fig. 3 ③).
- The center of this cylindrical cloudy cavity is then lifted up and becomes thicker and thicker; however, its sides keep attached to the hydrofoil surface. This "head" of the cloudy cavity will be dragged further downstream than the "legs" that are attached to the surface (see Fig. 3 ④).
- The head is lifted even higher and dragged even further downstream, and the legs move toward the midspan (see Fig. 3 ⑤). The cylindrical cloudy cavity then finally develops into a horseshoe shape or U-shape structure.

Three stages of a typical horseshoe-shaped cloudy cavity from breakoff to violent collapse were sketched by Kawanami et al. [34], as shown in Fig. 5. The bubbles contained in the cavity seem to get attracted toward the foil surface possibly by vortex stretching of the legs in the viscous boundary layer over the foil, and the horseshoe cavity is thereby split at the head. Then the remaining two legs of the horseshoe cavity collapse toward the foil surface, potentially causing local cavitation erosion.

It is also observed by Van Rijsbergen et al. [19] that the middle part of the cloud implodes and leaves two separate vortices on both sides of the foil. A comparison of the collapse of the horseshoe-shaped cloudy cavity between the experimental observations and the numerical results is shown in Fig. 6.

From the comparison between computation and experiment, it can be observed that the basic features of the collapse process are captured by the current URANS method, such as the collapse of the horseshoe cloudy cavity into two vortex structures on both sides and the shrinking and collapse of the remaining part toward the foil surface. However, Van Rijsbergen et al. [19] observed that the downstream attachment of the two legs of the horseshoe-shaped cloudy cavity was located further aftward than it is in the numerical prediction. Furthermore, the vortices stay most of the time intact rather than that they disappear completely at the end of the collapse, which is simulated by the current URANS method.

To study the effect of bubble number density on cavity extent and volume, a sensitivity study on the effect of the bubble number density has been conducted. It is observed from the results that a larger bubble number density than the default value ($n_b = 1e + 13$) did not produce significant effects on the extent and volume of vapor structures. However, a smaller bubble number density predicted a larger extent and volume of the vapor structures, and the peaks in the lift and drag became smaller. It is suggested by Sauer that this phenomenon could be ascribed to an overshoot in the source strength fluctuations, which is proportional to bubble number density. This overshoot seems an artifact of this cavitation model and is not associated with physics.

It is also noted that the measured pressure in the tunnel wall at 72 mm (1.2 chord length) upstream of the foil rotation center is adopted as the reference pressure for the calculation of the cavitation number rather than the experimental pressure at the outlet boundary. The thus-occurring difference in the position of the reference pressure results in a discrepancy of the cavitation number between the numerical simulation and the experiment. For further analysis, it is observed that a higher pressure is observed at the upstream station than at the outlet plane, resulting in a nondimensional difference of around $\Delta\sigma \approx 0.024$ (corresponding to 1.2%), showing that the current unsteady cavitation phenomena are

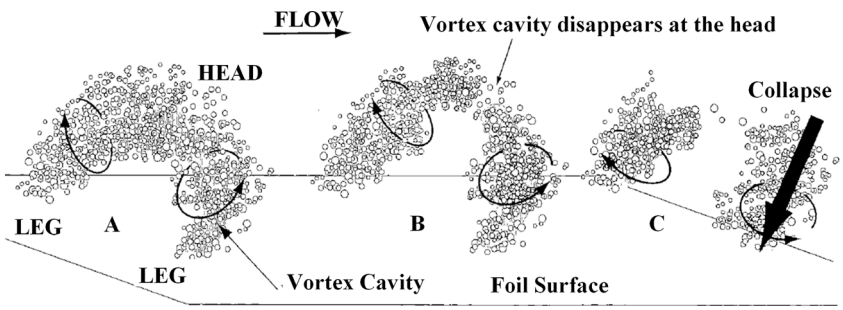

Fig. 5 Schematic diagram of the transformation process of a horseshoe cloudy cavity from break-off to violent collapse (Kawanami et al. [34])

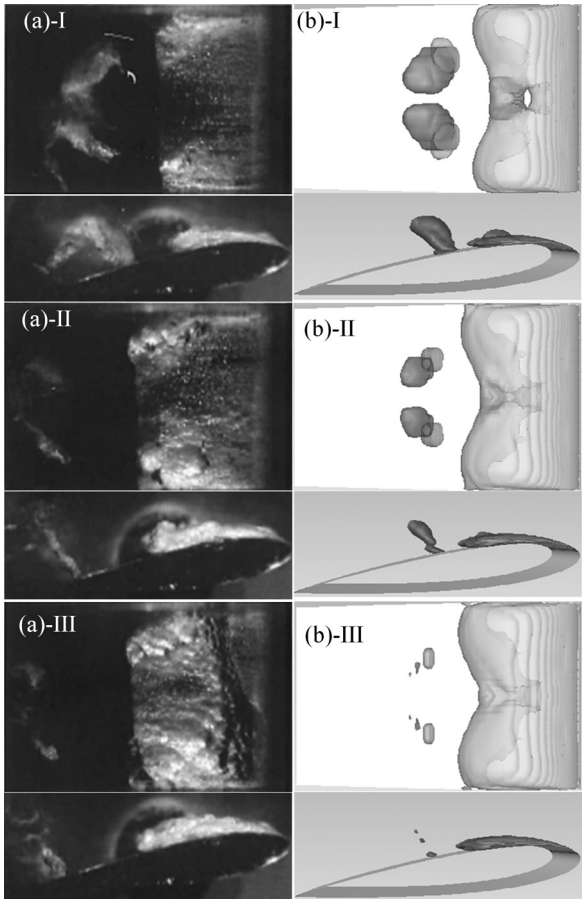

Fig. 6 Comparison of three typical instants during the collapse of the horseshoe-shaped cloudy cavity between the (*a*) experimental observations, and (*b*) numerical simulations (isosurface plots of the instantaneous vapor volume fraction with a contour value of $\alpha = 0.1$ for the flow over an NACA0015 hydrofoil (3D representation) with the modified SST k-ω turbulence model (flow from right to left, $C = 60$ mm, $AoA = 8$ deg, $\sigma = 2.01$, $U = 17.3$ m/s, $P_{out} = 302.295$ kPa, $T = 16.3\,^{\circ}$C)

simulated with a slightly higher cavitation number. However, this difference is so small that differences are expected to be within the numerical uncertainty and have no significant influence on the fundamental characteristics of the presented unsteady cavitation dynamics.

Although there is a discrepancy in the precise location and the extent of the vapor structures, it can be concluded that the observed collapse behavior qualitatively matches the experimental observations.

6 Assessment of Cavitation Erosion

6.1 Paint Test. For the NACA0015 hydrofoil at 8 deg angle of attack, the erosion result that is recorded after reapplication of the paint and two observation runs (nos. 26 and 27 from Ref. [19]) is shown in Fig. 7. It is indicated that the high impacts can be mainly attributed to two types of events similar to those found by Schmidt et al. [36] with evaluation of high static pressure peaks during a shedding cycle for the flow over a 3D twisted hydrofoil:

- The collapse of the substructures that are separated from the main sheet cavity (see the region in the rectangle)
- The collapse of the primary cloudy cavity directly shed from the main sheet cavity, related to the damaged area in the ellipse

The erosion result recorded for a different case, the NACA0018-45 hydrofoil at 6.5 deg angle of attack [24], is shown

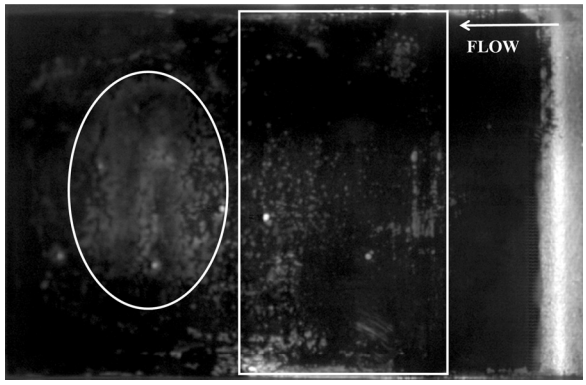

Fig. 7 Paint test result after re-application of paint and run no.26 and 27 ($C = 60$ mm, $\sigma = 2.01$, $U = 17.3$ m/s) on an NACA0015 hydrofoil at 8 deg angle of attack (30–60 min)

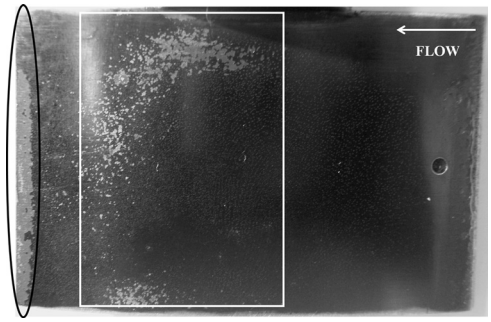

Fig. 8 Paint test result on an NACA0018-45 hydrofoil at 6.5 deg angle of attack ($C = 60$ mm, $\sigma = 0.72$, $U = 24.2$ m/s) after 45 min

in Fig. 8. It can be observed that the eroded area is mainly located on the second half of the hydrofoil surface and the trailing edge, as indicated by frames in Fig. 8. Based on observations by high-speed cameras, the erosion can be attributed to intensive unsteady phenomena, which are mainly associated with the collapse of the horseshoe-shaped cloudy cavity and the collapse of cloudy cavities near the trailing edge.

6.2 Numerical Evaluation. From an energy consideration, it is suggested that the process of focusing of potential energy that is contained in a macrocavity may lead to high values of the impact loads, which are supposed to be related to the impulsive pressure pulses produced during the breakup and collapse process.

The potential energy E_{pot} of the macrocavity at the start of the collapse can be written as (see also Bark et al., [11])

$$E_{pot} = \int (p - p_v) dV_v \tag{12}$$

where V_v is the vapor volume, and p and p_v are the surrounding pressure and the vapor pressure, respectively. Since it is not the energy that determines the erosion intensity, but rather the energy per unit time that is converted from potential energy into acoustic energy, it is the potential power that forms the basis of cavitation aggressiveness [7,10,20,37–39].

If we substitute the surrounding pressure p by the surface averaged pressure $\overline{p}$, the potential power P_{pot} for the cluster of bubbles can then be written in the following way:

$$P_{pot} = \frac{dE_{pot}}{dt} = \sum_{i=1}^{N} (\overline{p}_i - p_v) \frac{\partial V_{v_i}}{\partial t} + \sum_{i=1}^{N} \frac{\partial \overline{p}_i}{\partial t} V_{v_i} \tag{13}$$

where $\overline{p}_i$ and V_{v_i} represent the surface averaged pressure and vapor volume for the ith cell, and N is the total number of the

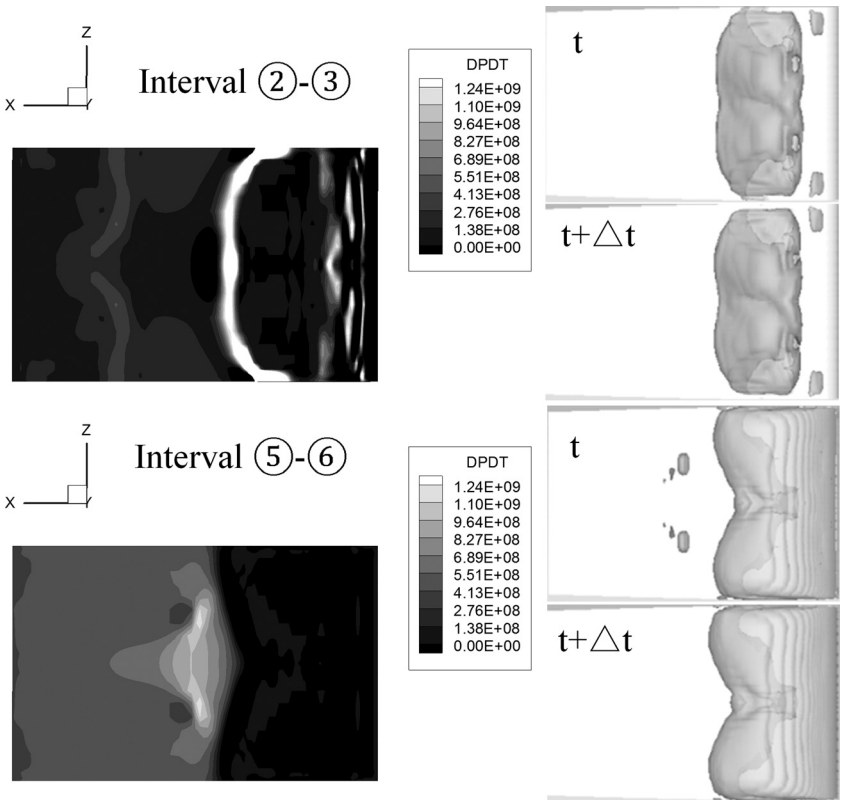

Fig. 9 Contours of $\partial p/\partial t$ at the moment when its maximum value is observed for two intervals and corresponding plots of the vapor volume fraction with an iso-value of $\alpha = 0.1$ at the relevant time points

discretized cells in the macro cavity. As the vapor volume for the ith cell can be replaced by the product of its vapor volume fraction α_i and the volume of the macrocavity V_c, i.e., $V_{vi} = \alpha_i V_c$, Eq. (13) can be written as follows:

$$P_{\text{pot}} = \sum_{i=1}^{N} (\overline{p_i} - p_v) \frac{\partial \alpha_i}{\partial t} V_c + \sum_{i=1}^{N} \frac{\partial \overline{p_i}}{\partial t} \alpha_i V_c \tag{14}$$

It should be noted that the first term in the right-hand side of Eq. (14) only contributes near the liquid-vapor interface since the time derivative of vapor volume fraction $\partial\alpha/\partial t$ is nonzero only there.

According to the above analyses, it is suggested that the instantaneous pressure p and its time derivative $\partial p/\partial t$ and the time derivative of vapor volume fraction $\partial\alpha/\partial t$ could determine the erosive risk factors. To qualitatively assess the risk of cavitation erosion, the evaluations are carried out only on the foil surface, which could be taken as the final result of the collapses of the cavities. Based on a sensitivity study of the two terms in Eq. (14) [20], it was concluded that the variation of the local pressure in time $\partial p/\partial t$ shows the best correlation with damaged regions by erosion on an NACA0015 hydrofoil at 8 deg angle of attack. Adding a term with the changes in vapor fraction $\partial\alpha/\partial t$ did not improve this correlation. Once the relevant terms in the potential power equation were assessed, the threshold level to distinguish between events that do and that do not contribute to the cavitation erosion damage function I_{Erosion} ($_{\text{Eq.}}$ (16)) was empirically determined. It is expected that there is a relation between this threshold, the grid density and the time step but that this sensitivity is limited for a well-resolved grid with time steps leading to Courant numbers between 0.5 and 1.0.

6.3 Rate of Pressure Rise. The rate of pressure rise ($\partial p/\partial t$) over the NACA0015 hydrofoil at the intervals between the six specific instants shown in Fig. 3 is examined in this section. It should be noted that the partial differential is estimated by using the first-order backward difference method:

$$\left.\frac{\partial p}{\partial t}\right|_{t+\Delta t} = \frac{p|_{t+\Delta t} - p|_t}{\Delta t} \tag{15}$$

The maximum values of $\partial p/\partial t$ for different intervals between six typical instants during one typical shedding cycle (as shown in Fig. 3) are analyzed to explore the correlation between the high variation in time of the pressure and the unsteady phenomena.

Contours of the time derivative of the instantaneous local pressure ($\partial p/\partial t$) are compared with the contour plots of the instantaneous vapor volume fraction of $\alpha = 0.1$ at the relevant time points. It can be observed that the maximum value of $\partial p/\partial t$ observed during the interval between instants ② and ③ and the interval between instants ⑤ and ⑥ are found to be qualitatively in agreement with the damage caused by high impacts as observed from the paint test, as shown in Fig. 9.

The following observations are made:

- Interval between instants ② and ③: The maximum value of $\partial p/\partial t$ is around 1.21e+10 and occurs in the vicinity of sidewalls where the cavity disappears. High values are also observed in the area surrounding the cylindrical cloudy cavity especially in the closure region.
- Interval between instants ⑤ and ⑥: Relatively high values of $\partial p/\partial t$ can be observed at the center where the horseshoe cloudy cavity eventually collapses. The value of the maximum pressure time derivative is, however, one order smaller than the $\partial p/\partial t$ value in the first time interval, causing a response over a broad area downstream of the horseshoe-shaped cavity.

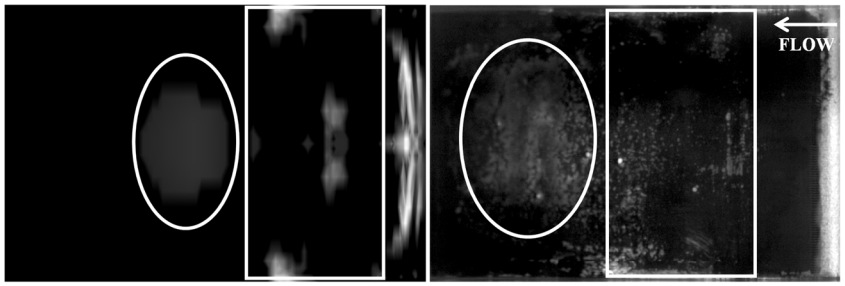

Fig. 10 Comparison between (*a*) a high erosion risk predicted by Eq. (16) with a threshold value of 3e +09 and (*b*) the damage area observed from paint tests (foil: NACA0015, *AoA* = 8 deg; flow from right to left). (*a*) Numerical results; (*b*) results from paint tests.

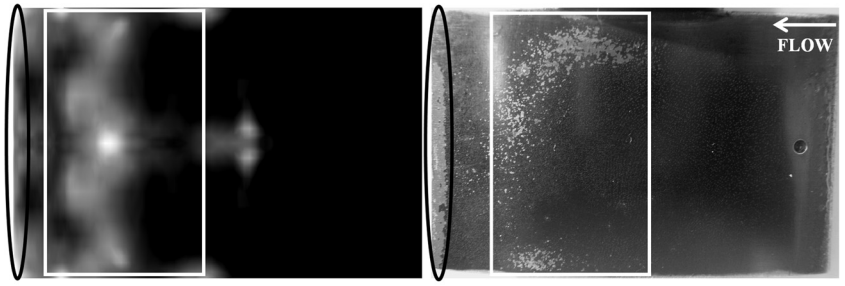

Fig. 11 Comparison between (*a*) a high erosion risk predicted by Eq. (16) with a threshold value of 7e +08 and (*b*) the damage area observed from paint tests (foil: NACA0018-45, *AoA* = 6.5 deg; flow from right to left) (*a*) Numerical results and (*b*) experimental results

The highest value of $\partial p/\partial t$ during the whole cycle is observed between instants ① and ②. It occurs when the remaining leading edge sheet cavity begins to collapse and detaches from the leading edge. However, no damage could be observed near the leading edge of the hydrofoil in the paint test. Although damage from the experiments could not be observed here because there was no paint applied at the leading edge, we would not expect erosive damage this close to the leading edge. A possible explanation for the simulated high pressure gradients might be that the URANS code gives a false overprediction of the unsteadiness of the sheet cavity in this area, which might be related to the difference in the onset of cavitation between a RANS model and the physics of experiments.

Apart from this leading edge region, the damaged region that is associated with high impacts can be successfully related to areas with large values of $\partial p/\partial t$ that are associated with the collapse of the substructures separated from the main sheet cavity and the horseshoe-shaped cavity. Moreover, the erosion damage located close to the sidewalls as recorded by the paint tests is also successfully captured from an analysis of $\partial p/\partial t$.

6.4 Erosion Intensity Function. It can be argued that erosion damage is not only dependent on the maximum value of one event but that it is a cumulative effect of the repeated loading on the material, as already suggested by Hammitt [37]. For this reason, it seems better to take the accumulated rate of pressure rise ($\partial p/\partial t$) for those values higher than a critical threshold value. This cumulative erosion intensity would, thus, not point toward the locations that are suffering from isolated peaks in pressure gradient only.

Therefore, an erosion intensity function is defined as follows:

$$I_{\text{Erosion}} = \frac{1}{N}\sum I_i \text{ and } I_i = \begin{cases} \dfrac{\partial p}{\partial t}; & \dfrac{\partial p}{\partial t} \geq \text{Threshold} \\ 0; & \dfrac{\partial p}{\partial t} < \text{Threshold} \end{cases} \tag{16}$$

where the subscript i refers to each individual time instant, determined by the selected time step size, and N is the number of the events with a value of $\partial p/\partial t$ higher than a certain threshold level.

It is indicated by the above Eq. (16) that a proper prediction of the cavitation erosion risk depends on the instantaneous local pressure gradient at each time step. Application of this equation results in a spatial distribution of the intensity function over the material surface.

Due to a lack of knowledge of the material properties of the foil's surface coating, a series of thresholds are applied to Eq. (16) for the evaluation of erosion intensity. It is found that when the threshold level becomes higher than a value in the order of 4e +09, the damage caused by the collapse of the horseshoe-shaped vapor structures will not be captured. A minimum level of the threshold level is found to be 1e +08 so as to avoid a situation where a high erosion risk is indicated over the complete hydrofoil surface.

Compared with the experimental results, the erosion intensity calculated with a threshold level of 3e +09 is found to best correlate with the damage regions observed from the paint test, as shown in Fig. 10. The regions with high values of I_{Erosion} in the white rectangle indicate the high impacts related to the collapse of the substructures that are separated from the main sheet cavity, and those in the white ellipse indicate the high impacts related to the collapse of the horseshoe-shaped cloudy cavity.

The discrepancies between the results from the erosion intensity function I_{Erosion} and the experimental observations can be ascribed to the discrepancies in the locations of the collapses of the shed cloudy cavity and the far smaller structures in the chordwise direction present in the experiments.

The applicability of this newly developed function is then examined further on an NACA0018-45 hydrofoil. It is found from this study, that the minimum threshold level to exclude the situation that the erosion risk is distributed all over the suction side is 7e +08. The erosion risk on the trailing edge of the hydrofoil will be smeared out with an increasing threshold and will disappear when it reaches 2e +10. Compared with the experimental results, the erosion intensity calculated with a threshold level of 7e +08 is

found to best correlate with the damage regions observed from the paint test, as shown in Fig. 11. The regions with high values of I_{Erosion} in the white rectangle indicate the high impacts related to the collapse of the horseshoe-shaped cloudy cavity, and those in the black ellipse indicate the high impacts related to the intensive collapse of the cavities near the trailing edge.

It has been concluded from this study that the erosion intensity function I_{Erosion} provides a better criterion to assess the cavitation erosion risk than the time-averaged value of the derivative of the local pressure $\partial p/\partial t$. An appropriate threshold level for the initial accumulation is critical for the final result, which is supposed to depend on the material properties only.

7 Conclusions

The following conclusions are drawn from this study:

- A realistic dynamic shedding of the sheet cavitation is only obtained after attenuating the eddy viscosity in the region with higher vapor volume fractions in the multiphase URANS method implemented in FLUENT. It seems that the modified turbulence model is less dissipative, thereby avoiding too much energy dissipation in the highly unsteady flow.
- For the unsteady simulations, the number of iterations per time step should be carefully selected to avoid a lack of numerical convergence since this may result in a significant influence on the shedding frequency. It is suggested that convergence is reached when the mass transfer rate does not change anymore with increased iteration number during each time step.
- The solutions are basically grid independent for the current grid resolution, even for the coarsest grid, where the maximum y^+ value on the foil surface is smaller than 1.0.
- It is believed that the effect of the vertical side wall boundary layer is an important reason that the horseshoe-shaped cloudy cavity develops.
- A new erosion intensity function (Eq. (16)) is proposed, based on the mean of peak values of the time derivative of the local pressure $\partial p/\partial t$ that exceed a certain threshold. This function provides a fair correspondence between the locations with the highest erosion risk from the computations and the damage areas obtained from the experiments. Further validation studies are recommended before this erosion intensity function can successfully be used for engineering studies.

Acknowledgment

The authors are grateful for the reports of the experiments provided by the Cooperative Research Ships (CRS), administered by MARIN. This work is also financially supported by the National Natural Science Foundation of China (Project No. 51309184) and the Programme of Introducing Talents of Discipline to Universities (Project No. B08031), China.

Nomenclature

C = chord length of the hydrofoil
E_{pot} = potential energy
E_a^{21} = approximate relative error $E_a^{21} = |1 - \phi_2/\phi_1|$
E_{ext}^{21} = extrapolated relative error
$E_{\text{ext}}^{21} = \left|1 - \phi_1/\phi_{\text{ext}}^{21}\right|$
$\phi_{\text{ext}}^{21} = ((h_2/h_1)^p \phi_1 - \phi_2/(h_2/h_1)^p - 1)$
$\text{GCI}_{\text{fine}}^{21}$ = fine grid convergence index
$\text{GCI}_{\text{fine}}^{21} = 1.25 E_a^{21}/((h_2/h_1)^p - 1)$
I_{Erosion} = erosion intensity
I_i = ith individual intensity
k = turbulence kinetic energy
n_b = bubble number density
N = number of events
p = local mixture pressure
p_v = vapor pressure
P_{pot} = instantaneous potential power
R = bubble radius
S_e = evaporation of the vapor bubbles
S_c = condensation of the vapor bubbles
u = velocity of the mixture
V_v = vapor volume
y^+ = nondimensional wall distance
α = vapor volume fraction
ε = dissipation rate of turbulent kinetic energy
μ_t = turbulent viscosity
$\rho_{m,l,v}$ = mixture, liquid, and vapor density
σ = cavitation number $\sigma = (p - p_v)/((1/2)\rho_l u^2)$
ω = specific dissipation rate of turbulent kinetic energy

References

[1] Berchiche, N., Franc, J. P., and Michel, J. M., 2002, "A Cavitation Erosion Model for Ductile Materials," ASME J. Fluids Eng., **124**(3), pp. 601–606.
[2] Brennen, C. E., 1995, *Cavitation and Bubble Dynamics*, Oxford University Press, Oxford, UK.
[3] Fortes-Patella, R., and Reboud, J. L., 1998, "A New Approach to Evaluate the Cavitation Erosion Power," ASME J. Fluids Eng., **120**(2), pp. 335–344.
[4] Wang, Y. C., and Brennen, C. E., 1999, "Numerical Computation of Shock Waves in a Spherical Cloud of Cavitation Bubbles," ASME J. Fluids Eng., **121**(4), pp. 872–880.
[5] Bensow, R. E., and Bark, G., 2010, "Implicit LES Predictions of the Cavitating Flow on a Propeller," ASME J. Fluids Eng., **132**, p. 041302.
[6] Kato, H., Konno, A., Maeda, M., and Yamaguchi, H., 1996, "Possibility of Quantitative Prediction of Cavitation Erosion Without Model Test," ASME J. Fluids Eng., **118**(3), pp. 582–588.
[7] Fortes-Patella, R., Reboud, J. L., and Briancon-Marjollet, L., 2004, "A Phenomenological and Numerical Model for Scaling the Flow Aggressiveness in Cavitation Erosion," EROCAV Workshop, Val de Reuil, France.
[8] Dular, M., and Coutier-Delgosha, O., 2009, "Numerical Modelling of Cavitation Erosion," Int. J. Numer. Meth. Fluids, **61**(12), pp. 1388–1410.
[9] Ochiai, N., Iga, Y., Nohmi, M., and Ikohagi, T., 2013, "Study of Quantitative Numerical Prediction of Cavitation Erosion in Cavitating Flow," ASME J. Fluids Eng., **135**(1), p. 011302.
[10] Van Terwisga, T. J. C., Fitzsimmons, P. A., Li, Z., and Foeth, E. J., 2009, "Cavitation Erosion—A Review of Physical Mechanisms and Erosion Risk Models," Proc. 7th Int. Sym. Cavitation, CAV2009, Ann Arbor, MI.
[11] Bark, G., Berchiche, N., and Grekula, M., 2004, *Application of Principles for Observation and Analysis of Eroding Cavitation-The EROCAV Observation Handbook*, 3.1 ed., Chalmers University of Technology, Goteborg, Sweden.
[12] Oprea, I. A., and Bulten, B., 2011, "Cavitation Modelling Using RANS Approach," WIMRC 3rd Int. Cavitation Forum 2011, University of Warwick, Coventry, UK.
[13] Hoekstra, M., and Vaz, G., 2009, "The Partial Cavity on a 2D Foil Revisited," Proc. 7th Int. Sym. Cavitation, CAV2009, Ann Arbor, MI.
[14] Li, D., Grekula, M., and Lindell, P., 2010, "Towards Numerical Prediction of Unsteady Sheet Cavitation on Hydrofoils," J. Hydrodyn., Ser B, **22**(5), pp. 741–746.
[15] Asnaghi, A., Jahanbakhsh, E., and Seif, M. S., 2010, "Unsteady Multiphase Modeling of Cavitation Around NACA0015," J. Mar. Sci. Tech., **18**(5), pp. 689–696.
[16] Reboud, J. L., Stutz, B., and Coutier-Delgosha, O., 1998, "Two Phase Flow Structure of Cavitation Experiment and Modeling of Unsteady Effects," Proc. 3rd Int. Sym. Cavitation, Grenoble, France.
[17] Coutier-Delghosa, O., Fortes-Patella, R., and Reboud, J. L., 2003, "Evaluation of the Turbulence Model Influence on the Numerical Simulations of Unsteady Cavitation," ASME J. Fluids Eng., **25**(1), pp. 38–45.
[18] Hoekstra, M., Van Terwisga, T. J. C., and Foeth, E. J., 2011, "SMP11 Workshop-Case 1: DelftFoil," 2nd Int. Sym. Marine Propulsors, Hamburg, Germany.
[19] Van Rijsbergen, M., Foeth, E. J., Fitzsimmons, P., and Boorsma, A., 2012, "High-Speed Video Observations and Acoustic-Impact Measurements on a NACA0015 Foil," Proc. 8th Int. Sym. Cavitation, CAV2012, Singapore.
[20] Li, Z., 2012, "Assessment of Cavitation Erosion With a Multiphase Reynolds-Averaged Navier–Stokes Method," Ph.D. dissertation, TUDelft, Delft, The Netherlands.
[21] Menter, F. R., 1994, "Two-Equation Eddy-Viscosity Turbulence Models for Engineering Applications," AIAA J., **32**, pp. 1598–1605.
[22] Schnerr, G. H., and Sauer, J., 2001, "Physical and Numerical Modeling of Unsteady Cavitation Dynamics," 4th International Conference on Multiphase Flow, New Orleans, LA.
[23] ANSYS, Inc, 2009, FLUENT Theory Guide (12.0), Providence, RI.
[24] Van Terwisga, T. J. C., 2009, "Criteria for Assessment of Cavitation Erosion Risk," CRS EROSION II Working Group, Proprietary.
[25] Celik, I., 2005, "Procedure for Estimation and Reporting of Discretization Error in CFD Applications," Internal Report, Mechanical and Aerospace Engineering Department, West Virgina University, Morgantown, WV.

[26] Celik, I., Klein, M., Freitag, M., and Janicka, J., 2006, "Assessment Measures for URANS/DES/LES: An Overview With Applications," J. Turbulence, **7**(48), p. N48.
[27] Sauer, J., 2000, "Instationär kavitierende strömungen - Ein neues modell, basierend auf front capturing (VoF) und blasendynamik," Ph.D. thesis, Karlsruhe University, Karlsruhe, Germany.
[28] Schnerr, G. H., Schmidt, S. J., Sezal, I. H., and Thalhamer, M., 2006, "Shock and Wave Dynamics of Compressible Liquid Flows With Special Emphasis on Unsteady Load on Hydrofoils and Cavitation in Injection Nozzles," *Proceedings of 6th International Symposium on Cavitation*, Wageningen, The Netherlands.
[29] Koop, A. H., 2008, "Numerical Simulation of Unsteady Three-Dimensional Sheet Cavitation," Ph.D. thesis, University of Twente, Enschede, The Netherlands.
[30] Oprea, I., 2009, "Wärtsilä CFD Results: 2D NACA0015 Foil," VIRTUE WP4 Workshop, Contribution From Wärtsilä.
[31] Hoekstra, M., and Vaz, G., 2008, "FreSCo Exercises for NACA0015 Foil," VIRTUE WP4 Workshop, Contribution From MARIN.
[32] Sorguven, E., and Schnerr, G. H., 2003, "Modified k-ω Model for Simulation of Cavitating Flows," Proc. Appl. Math. Mech., **2**(1), pp. 386–387.
[33] Li, Z., Pourquie, M., and Van Terwisga, T. J. C., 2011, "On the Assessment of Cavitation Erosion on a Hydrofoil Using Unsteady RANS," WIMRC 3rd International Cavitation Forum 2011, University of Warwick, Coventry, UK.
[34] Kawanami, Y., Kato, H., Yamaguchi, H., Maeda, M., and Nakasumi, S., 2002, "Inner Structure of Cloud Cavity on a Foil Section," JSME Int. J., **45**(3), pp. 655–661.
[35] Saito, Y. Y., Takami, R., Nakanori, I., and Ikohagi, T., 2007, "Numerical Analysis of Unsteady Behavior of Cloud Cavitation Around a NACA0015 Foil," Comput. Mech., **40**(1), pp. 85–96.
[36] Schmidt, S. J., Sezal, I. H., Schnerr, G. H., and Thalhamer, M., 2007, "Shock Waves as Driving Mechanism for Cavitation Erosion," Proceedings of the 8th International Symposium on Experimental and Computational Aerothermodynamics of Internal Flows, Lyon, France.
[37] Hammitt, F. G., 1963, "Observations on Cavitation Damage in a Flowing System," ASME J. Basic Eng., **85**(3), pp. 347–359.
[38] Nohmi, M., Iga, Y., and Ikohagi, T. 2008. "Numerical Prediction Method of Cavitation Erosion," Proceedings of FEDSM2008, Jacksonville, FL.
[39] Flageul, C., Fortes Patella, R., and Archer, A. 2012. "Cavitation Erosion Prediction by Numerical Cavitation," Proc. of 14th International Symposium on Transport Phenomena and Dynamics of Rotating Machinery, ISROMAC-14, February 2012, Honolulu, HI.